International Journal of Heat and Mass Transfer 61 (2013) 409–418

Contents lists available at SciVerse ScienceDirect

International Journal of Heat and Mass Transfer

journal homepage: www.elsevier.com/locate/ijhmt

Vapor chambers with jumping-drop liquid return from superhydrophobic condensers

Jonathan B. Boreyko, Chuan-Hua Chen *

Department of Mechanical Engineering and Materials Science, Duke University, Durham, NC 27708, USA

ARTICLE INFO

Article history:
Received 19 October 2012
Received in revised form 16 January 2013
Accepted 28 January 2013

Keywords:
Jumping drops
Vapor chamber
Superhydrophobicity
Wick
Interfacial resistance
Non-condensable gases

ABSTRACT

In closed-loop phase-change systems, self-propelled jumping drops on a superhydrophobic condenser offer a new mechanism to return the working fluid to the evaporator, eliminating the requirement for either external forces or wick structures along the return path. Here, we report the heat transfer performance of a jumping-drop vapor chamber consisting of two parallel plates, a superhydrophobic condenser and a superhydrophilic evaporator. With proper removal of the non-condensable gases including those dissolved in the working fluid, the overall thermal resistance of the jumping-drop chamber is primarily governed by the conduction resistance of the wicked evaporator in series with the interfacial resistances at the phase-change interfaces. The lumped resistance model was verified by systematically varying the parameters of the chamber such as wick thickness, vapor spacing, vapor temperature, and heat flux. As an alternative mechanism to transport the working fluid, the jumping drops can enable novel phase-change heat transfer systems such as planar thermal diodes and heat spreaders, for which this work provides practical design guidelines.

1. Introduction

Vapor chambers offer passive yet effective phase-change heat transfer in a planar form factor useful for microelectronics cooling [1–5]. Conventional vapor chambers are essentially flat-plate heat pipes [1–3], relying on wicked or grooved walls to return the working fluid from the condenser back to the evaporator by capillarity. For the capillary return to be effective, porous wick structures or fine grooves are required along the entire return path which poses design constraints and manufacturing complexities; see for example [6–9]. Alternative mechanisms such as gravitational and electrohydrodynamic return have their own limitations, rendering the heat transfer devices dependent on orientation or active power input [3]. Planar heat spreaders can also be obtained by arranging one-dimensional pipes such as thermosyphons and pulsating heat pipes into a plate [1,2], but such arrangements are less versatile because of the inherent one-dimensional tubular design, and are not effective for certain applications such as planar thermal diodes [10].

In our previous work [10], a novel jumping-drop mechanism for condensate return was utilized to enable an inherently planar vapor chamber, circumventing the drawbacks of gravity- or capillarity-driven return mechanisms. Rather than lining the entire vapor chamber with a wick structure, a wickless superhydrophobic plate was placed parallel to a wicked superhydrophilic plate, such that water condensing on the superhydrophobic surface would spontaneously jump across the gap directly back to the wicked evaporator (Fig. 1). The kinetic energy required for the jumping-drop phenomenon is harvested from the surface energy released upon coalescence [11–17], and the out-of-plane directionality is a result of the superhydrophobic surface breaking the symmetry of energy release [12,18].

Our jumping-drop chamber builds upon conventional vapor chambers with a few notable differences owing to the new liquid return mechanism. (i) The superhydrophilic evaporator design is directly borrowed from wicked vapor chambers, with the same capillary redistribution mechanism of the working fluid within the wick structures; however, the mass flow rate is no longer dictated by the cross sectional area of the wick (i.e. proportional to the thickness of the wick), but by the frequency and size distribution of the jumping condensate drops. The jumping return therefore circumvents the capillary wicking limit, which is typically the most significant limit of moderate temperature heat pipes and vapor chambers [1]. (ii) The perpendicular jumping return path between the condenser and the evaporator resembles the directionality of gravity-driven return in themosyphons; however, the jumping drops are much smaller and faster and therefore independent of gravitational orientation [12]. The out-of-plane jumping return is

* Corresponding author. Tel.: +1 919 660 5343; fax: +1 919 660 8963.
E-mail address: chuanhua.chen@duke.edu (C.-H. Chen).

0017-9310/$ - see front matter © 2013 Elsevier Ltd. All rights reserved.
http://dx.doi.org/10.1016/j.ijheatmasstransfer.2013.01.077

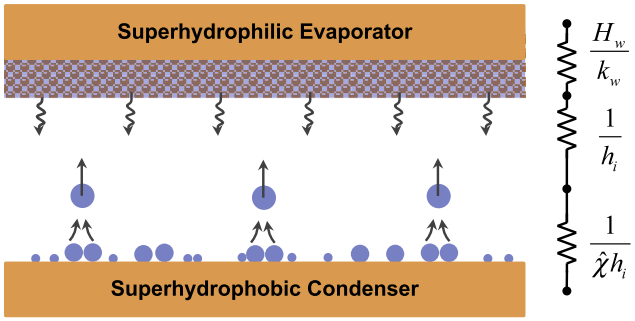

Fig. 1. Schematic of the jumping-drop vapor chamber consisting of a superhydrophobic evaporator and a superhydrophilic condenser in parallel. Heat is removed by evaporation of liquid water contained in the wicked evaporator, and rejected at the condenser by condensation of the water vapor. The working fluid is returned back to the evaporator by the self-propelled jumping phenomenon, where condensate drops spontaneously jump out-of-plane upon drop coalescence on the superhydrophobic surface. The major thermal resistances across the vapor chamber include the conduction resistance of the wick and the interfacial resistances across the evaporating and condensing interfaces.

scalable and particularly suitable for planar systems, unlike conventional vapor chambers with capillary return along wicked walls, where longer liquid return paths are expected for devices of larger areas. (iii) The jumping-drop vapor chamber consisting of condensers and evaporators of asymmetric wettability is a thermal diode by design [10], in contrast to conventional wicked vapor chambers with symmetric (interchangeable) condenser and evaporator.

Although the jumping-drop vapor chamber is essentially the forward mode of the jumping-drop thermal diode we previously reported [10], the work reported here represents a more systematic study of the heat transfer performance of vapor chambers enabled by the jumping-drop return mechanism. In particular, we carefully minimized the effects of non-condensable gases, and investigated the heat transfer coefficients while varying system parameters such as wick thickness, vapor spacing, vapor temperature, and heat flux. In this mechanistic study, we focused on the unique aspects of our jumping-drop vapor chamber. The inherently planar design justifies the simplification of the system as serial resistances due to wick conduction and interfacial phase change. The capability of the jumping drops to travel against gravity and/or vapor flow presents new operating limits to our vapor chamber.

2. Theoretical model

As schematically shown in Fig. 1, the jumping-drop vapor chamber consists of two parallel plates enclosing water in both liquid and vapor phases. The working fluid is circulated as follows: the liquid water evaporates from the wick structure embedded on the superhydrophilic evaporator, the water vapor condenses on the opposing superhydrophobic condenser, and the condensate jumps back to the evaporator upon drop coalescence. The parallel-plate configuration justifies the following one-dimensional model for the effective heat transfer coefficient and the operational limits specific to the jumping return.

2.1. Overall heat transfer coefficient

For phase-change heat transfer, non-condensable gases can present a significant thermal resistance due to their accumulation at the phase-change interface [19–21]. In the subsequent analysis, we assume negligible presence of non-condensable gases and ignore the associated gas diffusion resistance, in which case the interfacial resistance will predominantly govern the heat transfer at the phase-change interface. Kinetic theory yields an interfacial heat transfer coefficient [21],

$$h_i \approx \frac{2\hat{\alpha}}{2-\hat{\alpha}} \frac{\rho_v h_{lv}^2}{T_v} \sqrt{\frac{\bar{M}}{2\pi \bar{R} T_v}}, \tag{1}$$

where $\hat{\alpha}$ is the accommodation coefficient, ρ_v, h_{lv}, and $\bar{M}$ are the density, latent heat, and molecular weight of the saturated water vapor at a temperature T_v, and $\bar{R}$ is the universal gas constant. The accommodation coefficient is the fraction of molecular collisions that result in actual phase change across the interface, and is assumed to be equal for condensation and evaporation [21]. The accommodation coefficient ($\hat{\alpha}$) for water varies dramatically in different systems, and is reported to be typically below 0.1 for stagnant interfaces and above 0.1 for dynamically renewing interfaces [22]. Because of this large variation, the value of the accommodation coefficient is typically obtained by fitting the data measured on a particular phase-change system [22]. For a given $\hat{\alpha}$, the interfacial heat transfer coefficient (h_i) is approximately an exponential function of the vapor temperature.

For purely evaporative cooling on the superhydrophilic evaporator, the phase-change process is expected to be governed by the interfacial heat transfer coefficient in Eq. (1). For dropwise condensation on the superhydrophobic condenser, the phase-change heat transfer can be additionally affected by the capillary resistance (important for nanometric drops) and conduction resistance (important for millimetric drops) [20,21]. However, since the average diameter of self-propelled condensate drops on superhydrophobic surfaces tends to be micrometric [12], the interfacial resistance is expected to dominate on the condenser as long as non-condensable gases are negligible.

As shown in Fig. 1, the overall heat transfer coefficient of the jumping-drop vapor chamber (h_o) is dependent on the conduction resistance across the wick which is almost independent of temperature, and the interfacial resistances across the evaporator and condenser which strongly depend on the vapor temperature,

$$\frac{1}{h_o} \approx \frac{H_w}{k_w} + \frac{1}{h_i} + \frac{1}{\hat{\chi} h_i} \equiv \frac{H_w}{k_w} + \frac{1}{h_{pc}}, \tag{2}$$

where H_w is the thickness of the wick structure, k_w is the effective conductivity of the water-saturated wick, and $1/h_{pc}$ lumps together the phase-change resistances on both the evaporator and the condenser. The geometrical parameter $\hat{\chi}$ accounts for the partial coverage of dropwise condensate on the condenser surface and also the fact that the actual surface area of a drop open to additional condensation is larger than its projected area on the condenser. In this simplified model, we neglect the flow resistances for transporting the working fluid in both liquid and vapor phases, on the ground that the cross-sectional area for the fluid transport (the plate area) is very large and the distance of transport (the inter-plate spacing) is very short.

For our system, the geometrical parameter $\hat{\chi}$ is expected to be approximately constant and close to unity. The steady-state surface coverage is reached after the condensate drops start to coalesce and spontaneously jump; The surface coverage is expected to be constant for self-propelled condensation, e.g. around 40% for tests in the open air [12]. The actual surface area open to additional condensation is related to the projected surface area on the condenser by the apparent contact angle, which can be assumed constant for condensate drops with micrometric average diameter; For a contact angle of 90°, a factor of 2X is expected for hemispherical drops [23]. These two effects combine to yield an approximately constant $\hat{\chi}$ on the order of 1.

Combining Eqs. (1) and (2), the lumped heat transfer coefficient due to phase change on both the evaporator and the condenser is given by,

$$h_{pc} \approx \frac{\hat{\chi}}{1+\hat{\chi}} h_i \approx \hat{\beta} \frac{\rho_v h_{lv}^2}{T_v} \sqrt{\frac{\bar{M}}{2\pi \bar{R} T_v}}, \tag{3}$$

where the prefactor $\hat{\beta}$ absorbs both $\hat{\chi}$ and $\hat{\alpha}$,

$$\hat{\beta} \equiv \frac{\hat{\chi}}{1+\hat{\chi}} \frac{2\hat{\alpha}}{2-\hat{\alpha}}. \tag{4}$$

2.2. Jumping return limits

Compared to (flat-plate) heat pipes, the jumping-drop vapor chambers have some unique operating limits as a direct consequence of the new jumping return mechanism. For orientation independence, the jumping drops must be able to travel against gravity to reach the counter plate. At high heat fluxes, the jumping drops from the condenser must be able to additionally travel against the opposing vapor flow from the evaporator. We shall call the former the gravitational limit, and the latter the entrainment limit.

The jumping velocity of the merged liquid drop, u_l, follows the capillary-inertial scaling [12],

$$u_l \sim \sqrt{\frac{\sigma_{lv}}{\rho_l R_l}}, \tag{5}$$

where σ_{lv} is the liquid–vapor surface tension, and ρ_l and R_l are respectively the density and average radius of the condensate drops. Based on prior measurements of jumping condensate on a cooled superhydrophobic substrate exposed to the ambient air [12]: (i) The diameter of the condensate drops has a broad distribution, which has not yet been measured in an enclosed system with the non-condensable gases evacuated. (ii) Although the jumping velocity follows scaling Eq. (5), the prefactor can be well below unity; The measured jumping velocity is up to 20% of the theoretical capillary-inertial value, and vanishes for extremely small drops (perhaps due to viscous dissipation). Therefore, care should be exercised when applying Eq. (5).

The gravitational limit is reached when the separation between the condenser and evaporator plates (i.e. the vapor spacing H_v) exceeds a critical value, such that the jumping condensate cannot consistently return to the evaporator, leading to dryout in the "against gravity" orientation. The maximum jumping height against gravity is therefore given by,

$$H_v^G \sim \frac{u_l^2}{2g}, \tag{6}$$

where g is the gravitational acceleration.

The entrainment limit is reached when the viscous drag exerted by the opposing vapor flow prevents the jumping drops from returning to the evaporator, leading to dryout regardless of the orientation. The critical heat flux (q^E) at the entrainment limit can be related to the critical vapor velocity (u_v^E) assuming that the heat is carried away solely by latent heat transfer, $q^E \sim \rho_v h_{lv} u_v^E$. The critical vapor velocity and critical heat flux can be estimated from the vapor spacing (H_v) assuming a Stokes drag on the liquid drop,

$$H_v \sim \frac{u_l^2/2}{6\pi \mu_v u_v^E R_l / \left(\frac{4}{3}\pi \rho_l R_l^3\right)} \sim \frac{u_l^2}{9} \frac{\rho_l \rho_v h_{lv} R_l^2}{\mu_v q^E}, \tag{7}$$

where μ_v is the viscosity of the vapor.

For a jumping drop vapor chamber with the vapor spacing designed close to the gravitational limit, $H_v \lesssim H_v^G$, the critical heat flux at the entrainment limit can be estimated by combining Eqs. (6) and (7),

$$q^E \sim \frac{2}{9} \frac{g \rho_l \rho_v h_{lv} R_l^2}{\mu_v}. \tag{8}$$

Note that the liquid velocity is not explicitly used in deriving the entrainment limit in Eq. (8), which is valid when the vapor spacing is close to the gravitational limit.

3. Experimental methods

The experimental methodology for constructing and testing the jumping-drop vapor chamber (Fig. 2) builds upon our previous work [10]. A major difference is the adoption of a better methodology to control/remove non-condensable gases, leading to much improved performance as discussed in Section 4.7. We also modified the setup to allow thermal characterization over a larger range of vapor temperature and heat flux.

3.1. Fabrication and characterization

Copper plates (Alloy 101, 390 W/m K) were first treated for desired wettability. The superhydrophobic surface was fabricated via the electroless galvanic deposition of silver nanoparticles [24] on the front face of a copper plate, followed by a monolayer coating of 1-hexadecanethiol (Fisher Scientific AC120521000). The superhydrophilic surface was obtained by depositing a sintered copper wick of 100 μm-diameter particles on the front face of another copper plate (Thermacore, Lancaster, PA), followed by an oxygen plasma treatment (Emitech K-1050X). Superhydrophilic plates with wick thicknesses of H_w = 0.25, 0.5, 1.0, and 2.0 mm were fabricated. The sintered copper wick had a porosity of approximately 50%, and when saturated with water had an effective thermal conductivity of k_w = 38 W/m K [25].

The parallel copper plates both had a cross-sectional area of A = 76 mm × 76 mm. The superhydrophilic plate had a thickness of 6.4 mm, and the superhydrophobic plate 16.2 mm (to accommodate the circulation of chiller fluid through the plate, see below). The cross-sectional areas of the superhydrophilic wick and the superhydrophobic coating were both A_w = 61 mm × 61 mm, leaving space around the perimeter for the surrounding square gasket. Note that these dimensions were chosen for the ease of laboratory

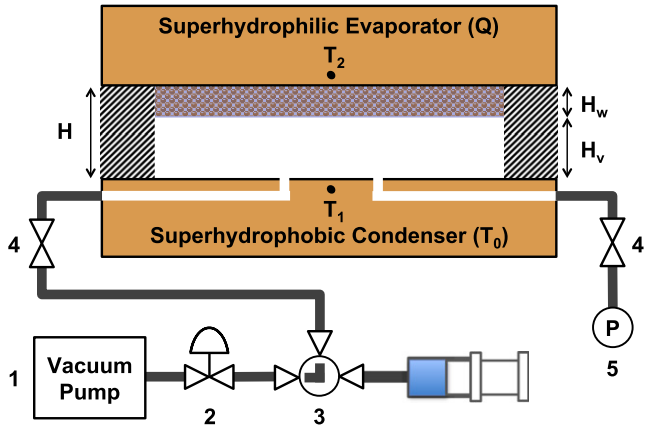

Fig. 2. Experimental setup for characterizing the vapor chamber. The vapor chamber consisted of an evaporator and a condenser in parallel that were separated by a rubber gasket with a thickness of H. The evaporator had a layer of porous wick with a thickness of H_w, leaving a vapor spacing of $H_v = H - H_w$. During the test, a total heat rate of Q was applied on the evaporator while the condenser was cooled by a circulating bath with a working fluid temperature of T_0; The resulting temperature drop across the vapor chamber was measured by the thermistors inserted into both plates. The components of the vacuum system included: (1) vacuum pump; (2) vacuum regulator; (3) three-way ball valve; (4) on/off valves; and (5) pressure gauge. A syringe was used for injecting water as the working fluid.

implementation. The jumping-drop vapor chamber can in principle be scaled to much larger areas.

The gasket made of water-resistant EPDM rubber (McMaster-Carr 8610K83/84/85, 0.1 W/m K) served four purposes: it defined the total separation between the parallel copper plates (H), provided a vacuum seal for the enclosed chamber, prevented water from traversing between the plates via the walls of the chamber, and thermally insulated the plates from each other. Through-holes were punched along the rubber gasket so that glass-filled nylon screws (McMaster-Carr 91221A225, 0.2 W/m K) could be used to seal the chamber air-tight. Three different gaskets with compressed thicknesses of H = 1.8, 2.5 and 3.7 mm were used to vary the vapor spacing between the plates ($H_v = H - H_w$).

Deionized water was injected to saturate the wick after the vapor chamber was sealed at atmospheric pressure. Water volumes of 1.0, 1.5, 2.5, and 4.25 mL were used for wick thicknesses of H_w = 0.25, 0.5, 1.0, and 2.0 mm, respectively. In each case, the amount of water injected exceeded the volumetric capacity of the wick by roughly 0.5 mL. The excess water helped to accommodate minor losses in the piping and from the subsequent vacuum pulls.

The assembled chamber was connected to a vacuum pump (Edwards RV3) on one side and a vacuum gauge (LJ Engineering DVG-2) on the opposite side. The digital vacuum gauge was accurate to ±0.34 kPa (0.1 inHg). An on/off valve was placed between the vacuum gauge and the vapor chamber to avoid prolonged exposure of the gauge to water vapor. A three-way ball valve was inserted between the vacuum pump and the vapor chamber, enabling the injection of the working fluid by a syringe. In selected experiments where a controlled amount of non-condensable gases was desired, a vacuum regulator (LJ Engineering 329-DP) was used between the pump and the three-way valve.

After the degassing procedures described in Section 3.2, the jumping-drop vapor chamber was tested at different orientations to investigate the potential dependence on gravity. For the condensate to jump along the direction of gravity (“with gravity”), the superhydrophobic condenser was placed on top and the evaporator at the bottom; For the condensate to jump “against gravity”, the chamber was flipped over with the superhydrophilic evaporator on the top. The “sideways” orientation was not tested in this work, since our previous work suggests that the “with” and ”against” orientations are sufficient to indicate any orientation dependence [10].

A uniform heat flux was imposed by a heater plate bolted onto the evaporator. The heater plate was made of copper with the same cross-sectional area (A) as that of the chamber. Three cartridge heaters rated 300 W each (Omega CIR – 1032/240) were inserted into the heater plate and controlled by a DC power supply (Ametek XG 300-5). To prevent heat leakage, the back side of the heater plate was insulated with a polyurethane foam (McMaster-Carr 85105K16, 0.1 W/m K). The heat was rejected at the condenser, with coolant circulated by a chiller (Neslab RTE 740) through tubes that were directly soldered into the condenser plate. With a maximum power of 750 W constrained by the cooling capacity of the chiller, the maximum heat flux across the wick area of A_w = 37 cm^2 was about 20 W/cm^2.

To measure the temperature drop (ΔT) across the chamber for a given power input (Q), two thermistors (Omega 44131) were inserted to measure the temperature on the condenser (T_1) and the evaporator (T_2). Contact resistances were minimized by a thermal paste (Marlow Industries 860-3079-002, 0.7 W/m K). As indicated by the small black dots in Fig. 2, the thermistor holes were drilled at H_p = 1 mm beneath the condenser surface and the evaporator surface on which the wick was sintered. For accurate measurement of the temperature drop between the condenser and evaporator surfaces, the ΔT's reported in this paper were all corrected for the temperature drop between the surfaces and the temperature probes. Assuming one-dimensional heat transfer within each solid plate, the corrected temperature drop was

$$\Delta T = T_2 - T_1 - \frac{2H_pQ}{k_{Cu}A_w}, \tag{9}$$

where H_p is the distance between the center of the thermistor hole and the surface to be probed, k_{Cu} is the thermal conductivity of the copper plates, and Q/A_w is approximately the heat flux through the active device area. Note that the corrected ΔT still includes the temperature drop across the thickness of the wick.

The overall heat transfer coefficient of the vapor chamber was calculated as

$$h_o = \frac{Q}{A_w\Delta T}, \tag{10}$$

where ΔT is the steady-state temperature drop across the chamber, measured as in Eq. (9) for a given power Q. In calculating the heat flux, $q = Q/A_w$, the wick area A_w is used instead of the total cross-sectional area A that includes the surrounding gasket, because the heat transfer is occurring predominantly within the inner chamber via phase change. The average vapor temperature in the chamber was estimated as,

$$T_v = \frac{T_2 + T_1}{2} - \frac{H_wQ}{2k_wA_w}, \tag{11}$$

where the last term accounts for the temperature drop across the wick.

3.2. Degassing procedures

A major improvement over our previous work [10] was the more effective removal of the non-condensable gases from the vapor chamber (Fig. 2). Two stages of evacuation were followed to ensure consistent removal of the vast majority of the non-condensable gases.

A primary vacuum was first pulled to remove the non-condensable gases from the vapor space. Before the primary vacuum, the vapor chamber was settled in thermal equilibrium with the working fluid of the chiller set at T_0 = 50 °C and the heater power set at 5.0 W, corresponding to a heat flux of 0.13 W/cm^2. The vapor temperature (T_v), taken as the average temperature of the evaporating and condensing surfaces, was approximately 52 °C. (The relatively large temperature drop at such a small heat flux was due to the presence of non-condensable gases.) For the primary vacuum, the chamber was simultaneously opened to the vacuum pump and gauge until a quasi-steady pressure of 13.6 kPa (−25.9 inHg gauge pressure) was obtained, equal to the saturation pressure of water vapor at 52 °C. To preserve the working fluid, the vapor chamber was closed off from both the pump and the gauge as soon as a quasi-steady pressure reading was reached. When a wet vacuum was pulled on the saturated chamber, the water vapor was continuously replenished by the water-soaked wick, unlike the non-condensable gases. For this reason, the chamber pressure could remain constant for a long period of time if left open to the vacuum pump.

To test the effectiveness of the primary vacuum, the same procedure was repeated at other vapor temperatures. The quasi-steady pressure reading always corresponded to the saturation pressure of the water vapor to within 1 kPa, an excellent agreement considering that the chamber was not strictly in thermodynamic equilibrium. With this one-to-one correspondence, the quasi-steady pressure reading represented the point at which the non-condensable gases had been predominantly evacuated, leaving mostly water vapor in the interstitial vapor space. However, the primary vacuum was not effective in removing the dissolved non-condensable gases.

Secondary vacuums were then pulled to remove non-condensable gases that were dissolved in the liquid water within the wick. To avoid further complicating the setup schematically shown in

Fig. 2, the working fluid was charged without degassing. Without secondary vacuums, the dissolved non-condensable gases would be gradually released into the vapor space during operation. Therefore, after this primary vacuum, the system was held at a higher temperature and larger heat flux to help drive out the non-condensables, typically for 30 min with the chiller fluid at $T_0 = 80$ °C and the heat power at 50 W (1.3 W/cm^2). The system was then returned back to steady state at $T_0 = 50$ °C and a lower heater power of 5 W, and a very brief secondary vacuum was then pulled to remove the newly released non-condensable gas. Note that the vacuum was always pulled at lower temperature and heat flux to avoid excessive loss of the working fluid. Secondary vacuums were repeated until the heat transfer performance reached a consistent peak performance that could not be further improved by additional vacuums.

3.3. Uncertainty analysis

The overall heat transfer coefficient (h_o) calculated in Eq. (10) is central to this study, and its measurement can be affected by two types of uncertainties: the run-to-run variations of the vapor chamber performance, and the measurement errors for temperature drop and heat flux. There is also some ambiguity in the active heat transfer area used for calculating the heat flux (q). However, as long as we consistently adopt the wick area (A_w), the trends in the calculated h_o should not be affected by this ambiguity.

To ensure consistent performance of the vapor chamber, the removal of the non-condensable gases was crucial. The run-to-run variation of the degassing procedures was relatively small, as long as the methodology outlined in Section 3.2 was followed on a vapor chamber with slightly overcharged working fluid. Note that the superhydrophilic evaporator could degrade after exposure to air, and was therefore retreated with oxygen plasma if exposed. The superhydrophobic surface tended to slowly deteriorate over time, in large part because the galvanically deposited silver particles on the superhydrophobic surface tended to come off during prolonged operation. However, obvious degradation was not observed within the test span of one to two weeks. If degraded, the condenser surface was polished and then retreated with the same superhydrophobic recipe. (This drawback can be eliminated by other routes to generate superhydrophobicity, but the simple galvanic recipe was adopted for this mechanistic study.)

The experimental uncertainty in ΔT measurements was ±0.03 °C, which was determined by inserting the two thermistors into a large mass of copper at a uniform temperature and sweeping the temperature from 0 °C to 80 °C. Because of the relatively large cross sectional area of the vapor chamber, less than 1% of the power (Q) supplied to the heater plate was estimated to leak through unintended paths, including conduction through the insulating foam and free convection and radiation through the sidewalls which were exposed to the ambient air.

The error bars in this paper were assessed based on the 95% confidence interval of independent measurements at selected conditions. The independence was ensured by preceding each measurement with a new charging and/or degassing procedure outlined in Section 3.2. These run-to-run uncertainties were larger than the aforementioned measurement errors of ΔT or Q.

4. Results and discussions

With water as the working fluid, the heat transfer performance of the jumping-drop vapor chamber depends on the following parameters:

- The design of the superhydrophilic evaporator, including the thermal conductivity (k_w), pore size (R_w) and thickness (H_w) of the wick;
- The design of the superhydrophobic condenser which affects the frequency and average diameter (R_l) of the jumping drops among other things;
- The spacing between the parallel condenser and evaporator (H_v);
- The applied heat flux (q) and the operating vapor temperature (T_v);
- The pressure of the non-condensable gases (P_{ncg}), if any.

Within the scope of this study, the condenser design was not varied because of the difficulty in visualizing jumping drops (including R_l) within the enclosed chamber, and the thermal conductivity (k_w) and pore size (R_w) of the wick were not varied due to limited availability (the wick was fabricated by an outside vendor). Except for these restrictions, we systematically varied other design parameters. With the exception of Section 4.6 on thermal rectification, the heat flux was always imposed on the superhydrophilic evaporator and rejected at the superhydrophobic condenser.

4.1. Effects of non-condensable gases

The non-condensable gases must be removed from the vapor chamber for effective phase-change heat transfer. To illustrate the dramatic effects of non-condensable gases, a vacuum regulator was used to control the non-condensable gas concentration (Fig. 3).

When non-condensable gases are at appreciable concentrations, their accumulation at the phase-change interfaces prohibits effective heat transfer. The more non-condensables, the less effective the phase-change thermal transport. These trends are apparent from the bottom three data series in Fig. 3. The charged vapor chamber was first heated to a vapor temperature of $T_v = 40$ °C, corresponding to a saturation pressure of approximately $P_v = 7$ kPa. The chamber was then progressively evacuated to total pressures of $P_t = 101$ kPa, 50 kPa and 25 kPa, corresponding to non-condensable gas pressures ($P_{ncg} = P_t - P_v$) of approximately 94 kPa, 43 kPa and 18 kPa, respectively. The vapor temperature was varied by sweeping the heat sink

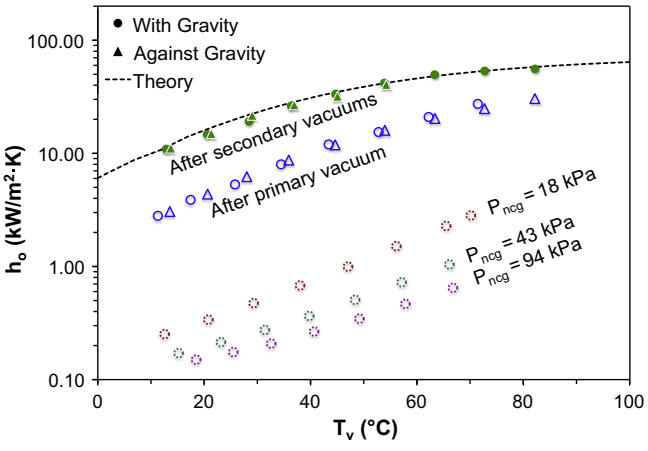

Fig. 3. Effects of non-condensable gases on the overall heat transfer coefficient (h_o) as a function of the vapor temperature (T_v), with the orders-of-magnitude variation shown by a semi-log plot. From bottom to top, the first three data series represent non-condensable gas pressures of $P_{ncg} = 94$ kPa, 43 kPa, and 18 kPa. The upper data series captured at both orientations represent the performance of the chamber after a primary vacuum only and the peak performance after secondary vacuums, respectively. The peak performance agrees well with the model (dashed line) according to Eqs. (2) and (3) with $\beta = 0.053$. All data are taken with $H_w = 0.5$ mm and $H_v = 2.0$ mm.

temperature (T_0) from 0 °C to 80 °C by 10 °C increments. Because of the large temperature drops associated with the poor heat transfer in the presence of non-condensables, the overall heat transfer coefficient was measured with a very small heat flux of $q = 0.3$ W/cm^2 ($Q = 10$ W).

The effects of primary and secondary vacuums outlined in Section 3.2 are illustrated by the top two data series in Fig. 3. Because of the more effective heat transfer with the majority of the non-condensables removed, a higher heat flux of $q = 1.3$ W/cm^2 ($Q = 50$ W) was applied in order to obtain a significant temperature drop. The heat transfer performance after the primary vacuum was slightly inferior to that after the secondary vacuums. Secondary vacuums were pulled repeatedly until additional evacuation could no longer improve the heat transfer performance, and the peak performance was recorded as the top data series in Fig. 3.

As shown in Fig. 3, the heat transfer performance of the properly degassed chamber was dramatically better after the non-condensables were rigorously removed. For this reason, subsequent measurements were always obtained after peak performances were achieved with sufficient number of secondary vacuums. Note that trace amounts of non-condensable gases could still remain in the system, but their contribution to the overall thermal resistance was expected to be negligible compared to other resistances modeled by Eq. (2). Indeed, the peak performance in Fig. 3 agrees very well with the model in Eq. (2), which neglects the non-condensable gas effects.

4.2. Wick thickness and conduction resistance

According to the simplified model in Eq. (2), the overall thermal resistance mainly consists of the conduction resistance through the thickness of the wick and the phase-change interfacial resistances. To test this model, the thickness of the wick was varied while its thermal conductivity was kept constant (Fig. 4). Wick structures with thicknesses of 0.5 mm, 1.0 mm and 2.0 mm were used. For each wick thickness, the heat flux was held constant at $q = 1.3$ W/cm^2 ($Q = 50$ W), and the vapor temperature was varied by sweeping the heat sink temperature from 0 °C to 80 °C. The results in Fig. 4 indicated better heat transfer performance at smaller wick thickness, confirming the importance of the conduction resistance across the wick.

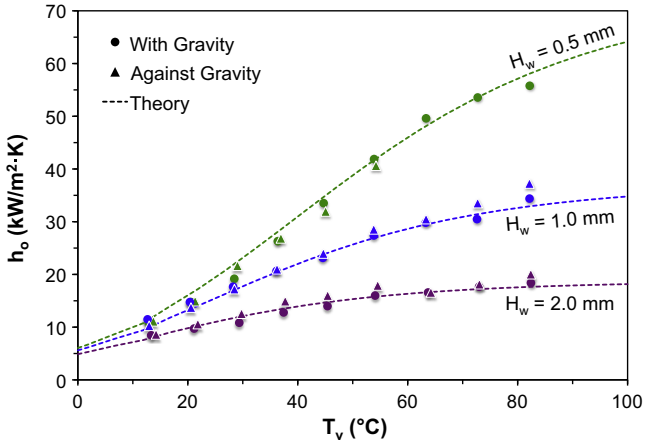

Fig. 4. The overall heat transfer coefficient (h_o) as a function of the vapor temperature (T_v), where the wick thicknesses is $H_w = 0.5$ mm, 1.0 mm, and 2.0 mm, and the corresponding vapor spacing is $H_v = 2.0$ mm, 1.5 mm, and 1.7 mm, respectively. The vapor chamber performance is orientation independent, except for the $H_w = 0.5$ mm wick at high vapor temperatures. The dashed lines are based on the lumped resistance model in Eqs. (2) and (3) with only one fitting parameter, $\hat{\beta}$, which is set as 0.053 for all theoretical curves in this paper.

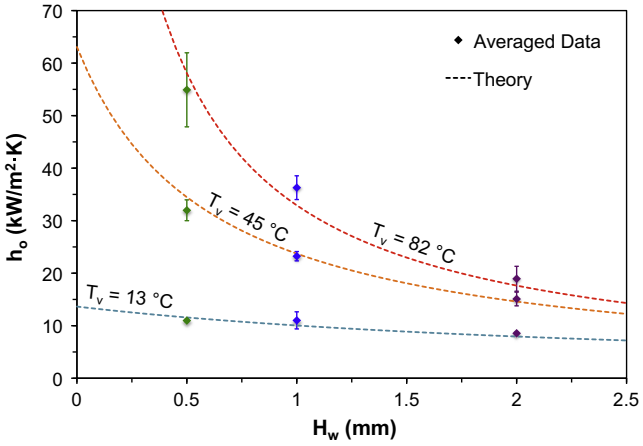

Fig. 5. The overall heat transfer coefficient (h_o) as a function of the wick thickness (H_w). The experimental data were measured at heat sink temperatures of $T_0 = 0$ °C, 40 °C, 80 °C at both orientations, except for the case of $H_w = 0.5$ mm and $T_0 = 80$ °C where reliable measurements could only be obtained "with gravity". The error bars represent 95% confidence intervals. The theoretical lines are plotted for an average vapor temperature of $T_v = 13$ °C, 45 °C, 82 °C, noting that T_v is slightly higher than T_0.

In Fig. 5, the overall heat transfer coefficients are plotted as a function of the wick thickness for selected heat sink temperatures (T_0). The performance agrees well with the theoretical model with $\hat{\beta} = 0.053$ and the vapor temperature (T_v) taken as the average measured T_v at a given T_0. Because of the extremely tedious measurements, error bars were only rigorously assessed for the data presented in Fig. 5. These error bars were representative of the experimental uncertainties for the parametric regime explored in this paper.

All three wick thicknesses demonstrated orientation-independent performance, except for the 0.5 mm case which had a slightly larger vapor spacing (and therefore gravitational dependence as discussed in Section 4.4). Although the performance can in principle be further improved with thinner wicks, other limits may come into play. At the same heat flux of 1.3 W/cm^2, steady-state results could not be obtained for the 0.25 mm wick due to dryout, likely due to an insufficient number of layers of 100 μm particles used to sinter all the wick structures used here.

4.3. Vapor temperature and phase-change resistance

The lumped phase-change heat transfer coefficient (h_{pc}) in Fig. 6 was deduced from experimental measurements according to Eq.

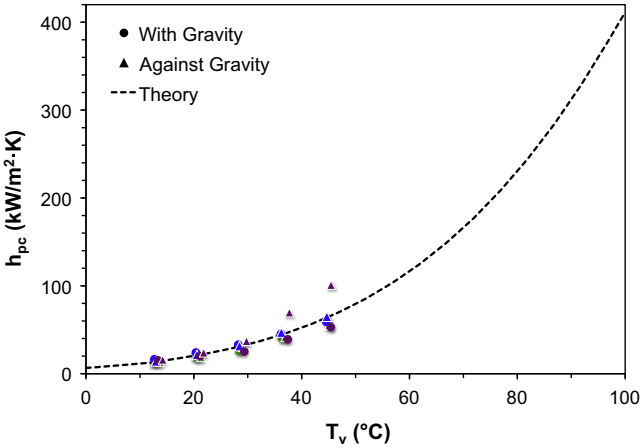

Fig. 6. The lumped phase-change heat transfer coefficient (h_{pc}) as a function of vapor temperature (T_v). The data are deduced from Fig. 4, and overlaid on the theoretical model in Eq. (3) with $\hat{\beta} = 0.053$.

(2), $1/h_{pc} = 1/h_o - H_w/k_w$. Based on the kinetic theory in Eq. (3), a nearly exponential dependence of h_{pc} on the vapor temperature is expected for phase-change processes. At low vapor temperatures, the phase-change heat transfer coefficients extracted from Fig. 4 were well modeled by Eq. (3). At vapor temperatures higher than 50 °C, the temperature drop across the phase-change interfaces was typically below 0.1 °C, in which case the extraction of h_{pc} was no longer reliable.

For all theoretical curves in this paper, a single fitting parameter of $\hat{\beta} = 0.053$ is consistently used. Among other possible combinations according to Eq. (4), this particular $\hat{\beta}$ value represents the reasonable combination of a geometrical parameter of $\hat{\chi} = 1$ and an accommodation coefficient of $\hat{\alpha} \approx 0.1$ (around the maximum attainable for "stagnant interfaces" [22]). The high accommodation coefficient used to fit the experimental data corroborates the effectiveness of our methodology in removing the non-condensable gases.

The trends in the overall heat transfer coefficient in Fig. 4 can now be fully explained. At low vapor temperatures (T_v), the overall thermal resistance ($1/h_o$) is dominated by the phase-change resistances ($1/h_{pc}$) which decreases exponentially with T_v. At higher temperatures, the vapor chamber is dominated by the wick resistance (H_w/k_w) which is nearly independent of T_v but strongly depends on the wick thickness (H_w).

4.4. Vapor spacing and gravitational dependence

To investigate the gravitational dependence, the vapor spacing was varied by changing the gasket thickness between the condenser and evaporator plates, and the resulting vapor chamber was tested at both "with gravity" and "against gravity" orientations (Fig. 7). Note that the vapor spacing (H_v) was obtained by deducting the wick thickness (H_w) from the inter-plate spacing (H) defined by the compressed gasket thickness. With the wick thickness fixed at $H_w = 1.0$ mm, the vapor spacing was varied with $H_v = 0.8$, 1.5, and 2.7 mm. In the "with gravity" orientation, the overall heat transfer coefficient was equivalent for all three vapor spacings, consistent with the independence to H_v implied in Eq. (2). In the "against gravity" orientation, however, dryout occurred consistently with $H_v = 2.7$ mm, indicating that a large portion of the condensate drops could not jump back to the evaporator.

Although the threshold vapor spacing for the gravitational dependence was difficult to pinpoint, it should be around 2.0 mm based on tests plotted in Fig. 4. With the conditions indicated in Fig. 4, dryout never occurred for the slightly smaller vapor spacing of $H_v = 1.5$ mm and 1.7 mm at both orientations. For $H_v = 2.0$ mm, dryout did not occur in the "with gravity" orientation, but occurred in the "against gravity" orientation at somewhat random times during the testing, typically at very high vapor temperatures. These observations indicate that a vapor spacing of 2.0 mm was around the borderline for the loss of orientation independence.

According to Eq. (6), the gravitational limit of $H_v^G \approx 2.0$ mm corresponds to a condensate drop velocity of $u_l \sim 0.2$ m/s. From this estimate of the jumping velocity, the average diameter of the jumping drops is of order $R_l \sim 100$ μm based on Eq. (5) with a 20% prefactor. These estimates are consistent with our earlier measurements, albeit in open air [12].

4.5. Effects of heat fluxes

Up to now, the heat transfer performance of the degassed chamber was measured at a fixed heat flux of 1.3 W/cm^2. This low heat flux was useful to ensure reliable thermal measurements over a large parametric space. However, the jumping-drop vapor chamber may experience much higher heat fluxes in real applications. We now report the effects of increasing heat fluxes, up to the instrumentation limit of 20 W/cm^2.

At low heat fluxes, the overall heat transfer coefficient (h_o) for a given vapor temperature (T_v) was essentially independent of the heat flux (Fig. 8). For heater powers of $Q = 25$, 50, and 100 W (corresponding to $q = 0.7$, 1.3, and 2.7 W/cm^2), h_o was independent of the heat flux for a wide range of vapor temperature from 10 ° to 85 °, obtained by varying the temperature of the chiller fluid (T_0). This independence to low heat fluxes is crucial for supporting the adequacy of our model for the overall heat transfer coefficient.

At higher heat fluxes, the overall heat transfer coefficient became dependent on the heat flux. In Fig. 9a, the heat sink temperature was held constant at $T_0 = 25°$, and the heater power was increased from 50 W to 750 W (1.3 to 20 W/cm^2). In Fig. 9b, the data set in Fig. 9a is replotted and compared against the 50 W data set from Fig. 8. The overlap of the two data sets suggests that the dependence on heat flux is partly due to the variation of vapor temperature, resulting from the variation of heater power at constant T_0. The remaining discrepancy at high heat fluxes may be attributed in part to an increased interfacial heat transfer coefficient (h_i), owing to an increased number of active nucleation sites at both the condenser and the evaporator and therefore an increased accommodation coefficient ($\hat{\alpha}$); See for example [20,26].

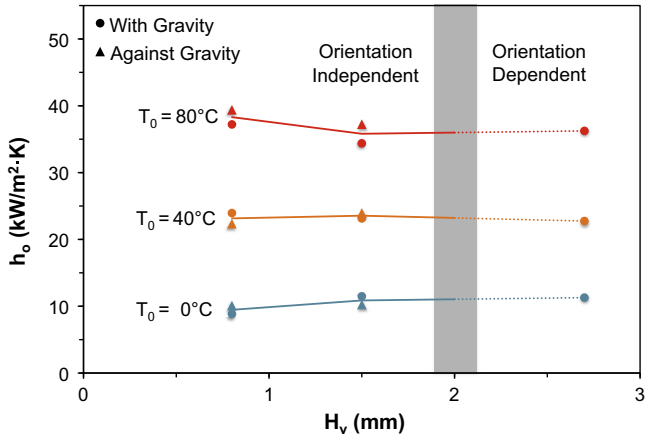

Fig. 7. The overall heat transfer coefficient (h_o) as a function of the vapor spacing (H_v). For relatively small vapor spacing, h_o is essentially independent of H_v regardless of the orientation. Above a critical limit of $H_v^m \approx 2.0$ mm, however, dryout occurs in the "against gravity" orientation and only the "with gravity" data can be reliably obtained. All data are taken with $H_w = 1$ mm and $q = 1.3$ W/cm^2.

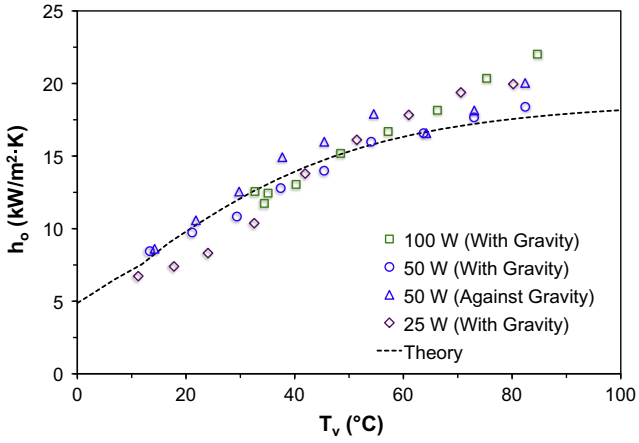

Fig. 8. At small heat fluxes, the overall heat transfer coefficient (h_o) for a given vapor temperature (T_v) is independent of the heat flux (q). For small heater powers up to $Q = 100$ W ($q = 2.7$ W/cm^2), the h_o versus T_v trend agrees well with the model over a wide range of vapor temperature. All data are taken with $H_w = 2$ mm and $H_v = 1.7$ mm.

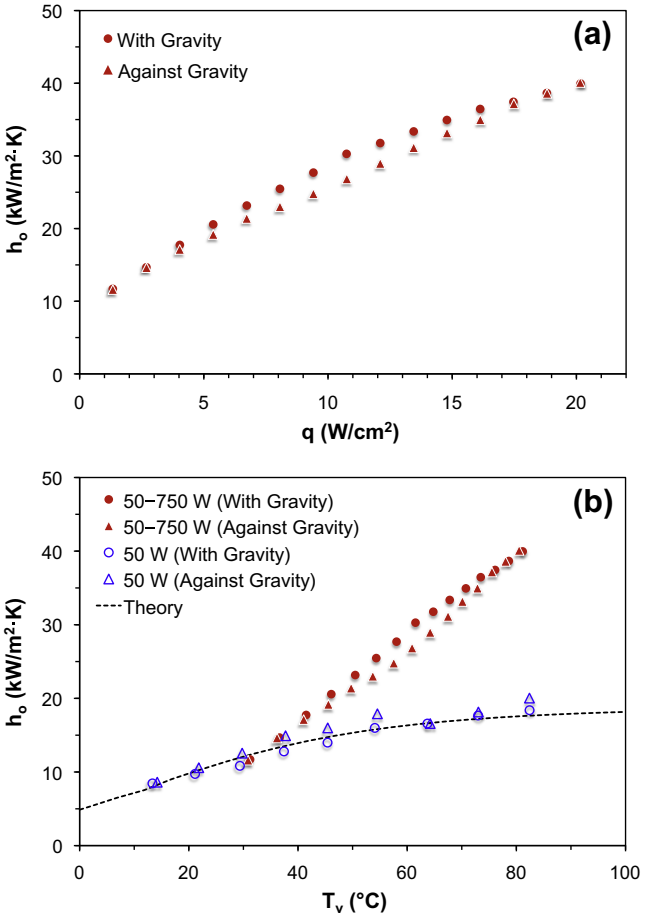

Fig. 9. The overall heat transfer coefficient (h_o) as a function of (a) the imposed heat flux (q); and (b) the vapor temperature (T_v). At low heat fluxes, h_o is only a function of the vapor temperature. At high heat fluxes, h_o is function of both the vapor temperature and the heat flux. The data in (a) are obtained with the heat sink temperature held at T_0 = 25 °C and the heater power (Q) varied from 50 W to 750 W at 50 W increments. The data in (a) are replotted in (b) together with the 50 W-data from Fig. 8. All data are taken with H_w = 2 mm and H_v = 1.7 mm.

In Fig. 9a, the jumping-drop vapor chamber was found to be stable and orientation-independent all the way up to 20 W/cm^2, a limit artificially posed by the cooling capacity of the chiller. Our results suggest that the entrainment limit was not encountered at the tested range of heat fluxes, consistent with the scaling estimate from Eq. (8). With H_v = 1.7 mm $\approx H_v^G$ and $R_l \sim 100$ μm from Section 4.4 as well as the vapor properties at 80°C, the critical heat flux at the entrainment limit should be on the order of $q^E \sim 100$ W/cm^2, well above the tested range.

4.6. Thermal rectification

The jumping-drop vapor chamber consisting of two parallel plates with asymmetric wettability can be exploited for thermal rectification [10]. In previous subsections, we have shown that a heat flux imposed on the superhydrophilic surface can be effectively removed via phase-change heat transfer (the forward mode). If the direction of the heat flow is reversed and the superhydrophobic surface is heated instead, no latent heat transfer is expected (the reverse mode).

The thermal rectification by the jumping-drop vapor chamber is well conveyed by the following comparison in Fig. 10: In the forward mode with an average $T_2 - T_1$ = 2.0 °C, a heat flux of 8.1 W/cm^2 was transported from the hotter superhydrophilic surface to

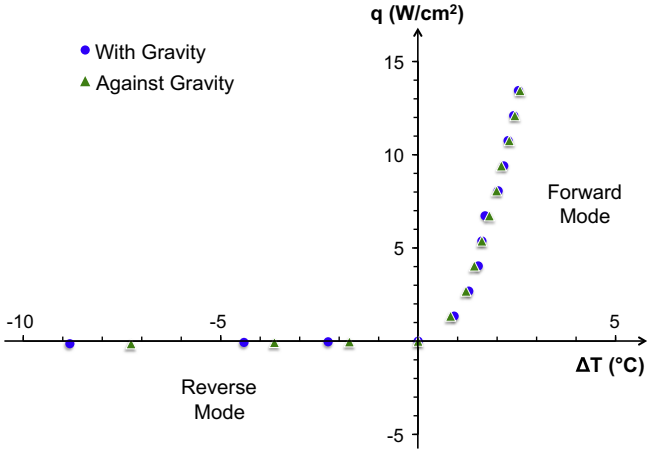

Fig. 10. The jumping-drop vapor chamber is inherently a thermal diode, transporting heat effectively only when the superhydrophilic surface is hotter than the superhydrophobic one, i.e. in the forward mode with $\Delta T > 0$. The forward-mode data are collected on a properly degassed vapor chamber. The reverse-mode data are extracted from Fig. 3 in [10], since non-condensable gas effects are only prominent in the forward mode with phase-change heat transfer. The heat fluxes are calculated by dividing the heat rate with the wick area ($q = Q/A_w$). All data are taken with H_w = 1.0 mm, H_v = 1.5 mm, and T_0 = 25 °C.

the colder superhydrophobic one; In the reverse mode with an average $T_2 - T_1 = -2.0$ °C, only 0.033 W/cm^2 was transported in the opposite direction. This ratio of forward and reverse heat flux under otherwise identical conditions yields a rectification coefficient (diodicity) of approximately 250. Despite the slight dependence on orientation in the reverse mode, likely due to free convection within the chamber, the forward mode was independent of orientation.

4.7. Comparison with prior results

In Fig. 11, our prior results measured on a vapor chamber with approximately 3 kPa of non-condensable gases [10] are compared against the new results following the rigorous degassing procedures in Section 3.2. To facilitate the comparison, the effective thermal conductivities in the forward mode (k_f) used in [10] is converted to the overall heat transfer coefficients (h_o) by $h_o = (k_f/H)(A/A_w)$, where H is the total septation between the two plates and A/A_w is the ratio of the plate area to the wick area. The overall heat transfer coefficient is a better indication of the vapor chamber performance, which is evident in Fig. 7 by the insensitivity of the heat transfer coefficient to the vapor spacing. From the comparison, it is evident that trace amounts of non-condensable gases could dramatically affect the performance of the vapor chamber, an observation consistent with Fig. 3.

Careful removal of the non-condensable gases also eliminated the premature onset of boiling we previously observed [10]. With non-condensable gases remaining in our previous system, boiling appeared to have occurred at 1.3 W/cm^2 or even lower heat fluxes. The premature onset of boiling was indicated by the sudden increase in the heat transfer coefficient at vapor temperatures above 50 °C and the simultaneous loss of orientation independence (Fig. 11). The premature boiling in our previous system was also consistent with the lack of secondary vacuums, which were primarily responsible for removing the non-condensable gases (boiling nuclei) dissolved in the working liquid. With the new degassing procedure, no boiling was observed at vapor temperatures exceeding 80 °C, and the heat transfer performance was independent of orientation for heat fluxes up to the instrumentation limit of 20 W/cm^2.

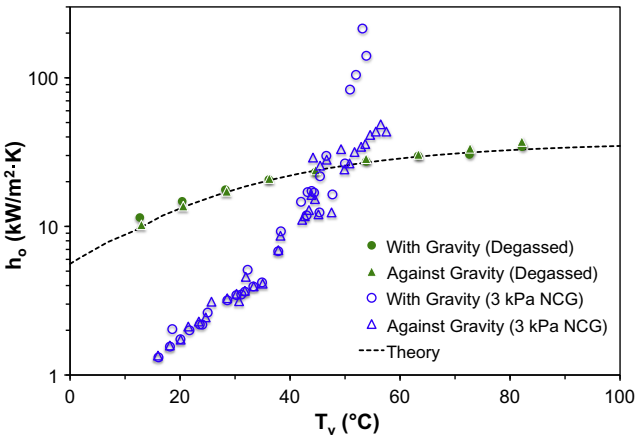

Fig. 11. Comparison of a degassed vapor chamber with an otherwise identical chamber containing approximately 3 kPa of non-condensable gases (NCG). The performance of the degassed chamber was measured at a power of $Q = 50$ W, and the 3 kPa-data are extracted from Fig. 4 in [10] with $Q = 30$–90 W. Both vapor chambers used $H_w = 1.0$ mm and $H_v = 1.5$ mm. The dotted line represents the model of the overall heat transfer coefficient with negligible non-condensable gases.

We previously reported an orientation-independent upper limit to the effective thermal conductivity, $k_f^m \approx k_w(A_w/A)(H/H_w)$, beyond which the gravitational independence is lost; See Eq. (2) in [10]. This limit is equivalent to an upper limit of the overall heat transfer coefficient that is orientation independent,

$$h_o^m \approx \frac{k_w}{H_w}. \tag{12}$$

Compared to the overall thermal resistance model in Eq. (2), it is apparent that the orientation-independent upper limit in Eq. (12) is reached when the conduction resistance is much larger than the interfacial resistances. As shown in Fig. 11, the upper limit can be reached either at the onset of boiling as in our previous report, or at very large vapor temperatures as in the present paper.

4.8. Discussions

A few limitations of our work are noteworthy. First, We used water as the working fluid for this mechanistic study, but other working fluids are in principle possible, e.g. by adopting superoleophobic condensers via surface patterning (see for example [27]) or using working fluids of large surface tension (mercury condensate can jump upon coalescence on a flat surface [28]).

Second, the jumping return mechanism was not studied in situ because of the opaque device construction. Such a study is highly desirable for identifying the size distribution and jumping frequency of the condensate drops in an evacuated chamber (e.g. by including a transparent superhydrophobic surface [29]). A direct measurement of the jumping return process will help elucidate the experimentally identified gravitational limit, where the jumping drops were able to travel approximately 2 mm against gravity.

Third, the heat transfer coefficient associated with the self-propelled dropwise condensation on superhydrophobic surfaces was neither directly measured nor modeled from first principles. Based our experimental results and the theoretical fit, the superhydrophobic dropwise condensation can exhibit an effective heat transfer coefficient (h_c) well over 100 kW/m^2 K, perhaps approaching 1000 kW/m^2 K at high vapor temperatures. Note that h_c is lower bounded by the lumped phase-change heat transfer coefficient h_{pc} shown in Fig. 6 ($h_c \approx 2h_{pc}$ if $\hat{\chi} \approx 1$). In future work, these estimates should be reconciled with other measurements [30,31] after the condensation heat transfer is properly isolated.

Lastly, although we only tested the jumping-drop vapor chamber with a uniform heat flux of up to 20 W/cm^2 due to instrumentation limitations, we expect a much higher critical heat flux particularly with localized hotspots imposed on an optimized evaporator. Borrowing from the wick designs in flat-plate heat pipes, see for example recent work in [32–40], we expect to improve both the critical heat flux (e.g. using a wick with a smaller pore size or a bi-dispersed structure) and the effective heat transfer coefficient (e.g. using a wick with higher effective conductivity or smaller thickness).

5. Conclusions

Guided by simple scaling models, we have studied the heat transfer performance of jumping-drop vapor chambers. For optimal performance, the non-condensable gases including those dissolved in the working liquid should be carefully removed. Based on Eq. (2) which was supported by the experiments, the overall heat transfer coefficient of the degassed vapor chamber was dominated by the interfacial phase-change resistances at low vapor temperatures and the wick conduction resistance at high vapor temperatures. The jumping return mechanism imposed unique performance restrictions including the gravitational limit which was experimentally confirmed, and the entrainment limit which awaits further verification at higher heat fluxes. The jumping-drop vapor chamber was inherently a thermal diode with large rectification coefficients.

Acknowledgments

This work was supported by a DARPA Young Faculty Award (Contract No. N66001-10-1-4048) with A. Bar-Cohen and T. Kenny as technical mentors.

References

[1] G.P. Peterson, An Introduction to Heat Pipes: Modeling, Testing, and Applications, Wiley-Interscience, New York, 1994.
[2] A. Faghri, Heat Pipe Science and Technology, Taylor & Francis, New York, 1995.
[3] D. Reay, P. Kew, Heat Pipes, fifth ed., Butterworth-Heinemann, Oxford, 2006.
[4] I. Sauciuc, G. Chrysler, R. Mahajan, R. Prasher, Spreading in the heat sink base: phase change systems or solid metals?, IEEE Trans Compon. Pack. Technol. 25 (2002) 621–628.
[5] R. Mahajan, C.P. Chiu, G. Chrysler, Cooling a microprocessor chip, Proc. IEEE 94 (2006) 1476–1486.
[6] D.A. Benson, R.T. Mitchell, M.R. Tuck, D.W. Palmer, G.P. Peterson, Ultrahigh-capacity micromachined heat spreaders, Microscale Therm. Eng. 2 (1998) 21–30.
[7] R. Hopkins, A. Faghri, D. Khrustalev, Flat miniature heat pipes with micro capillary grooves, J. Heat Transfer 121 (1999) 102–109.
[8] Y. Wang, K. Vafai, An experimental investigation of the thermal performance of an asymmetrical flat plate heat pipe, Int. J. Heat Mass Transfer 43 (2000) 2657–2668.
[9] S. Kalahasti, Y.K. Joshi, Performance characterization of a novel flat plate micro heat pipe spreader, IEEE Trans. Compon. Pack. Technol. 25 (2002) 554–560.
[10] J.B. Boreyko, Y. Zhao, C.H. Chen, Planar jumping-drop thermal diodes, Appl. Phys. Lett. 99 (2011) 234105.
[11] C.H. Chen, Q. Cai, C. Tsai, C.L. Chen, G. Xiong, Y. Yu, Z. Ren, Dropwise condensation on superhydrophobic surfaces with two-tier roughness, Appl. Phys. Lett. 90 (2007) 173108.
[12] J.B. Boreyko, C.H. Chen, Self-propelled dropwise condensate on superhydrophobic surfaces, Phys. Rev. Lett. 103 (2009) 184501.
[13] C. Dietz, K. Rykaczewski, A.G. Fedorov, Y. Joshi, Visualization of droplet departure on a superhydrophobic surface and implications to heat transfer enhancement during dropwise condensation, Appl. Phys. Lett. 97 (2010) 033104.
[14] K. Rykaczewski, J.H.J. Scott, S. Rajauria, J. Chinn, A.M. Chinn, W. Jones, Three dimensional aspects of droplet coalescence during dropwise condensation on superhydrophobic surfaces, Soft Matter 7 (2011) 8749–8752.
[15] X. Chen, J. Wu, R. Ma, M. Hua, N. Koratkar, S. Yao, Z. Wang, Nanograssed micropyramidal architectures for continuous dropwise condensation, Adv. Funct. Mater. (2011) 4617–4623.
[16] R. Enright, N. Miljkovic, A. Al-Obeidi, C.V. Thompson, E.N. Wang, Condensation on superhydrophobic surfaces: the role of local energy barriers and structure length scale, Langmuir 28 (2012) 14424–14432.

[17] M. He, X. Zhou, X. Zeng, D. Cui, Q. Zhang, J. Chen, H. Li, J. Wang, Z. Cao, Y. Song, L. Jiang, Hierarchically structured porous aluminum surfaces for high-efficient removal of condensed water, Soft Matter 8 (2012) 2680–2683.
[18] J.B. Boreyko, C.H. Chen, Self-propelled jumping drops on superhydrophobic surfaces, Phys. Fluids 22 (2010) 091110.
[19] W.J. Minkowycz, E.M. Sparrow, Condensation heat transfer in the presence of noncondensables, interfacial resistance, superheating, variable properties, and diffusion, Int. J. Heat Mass Transfer 9 (1966) 1125–1144.
[20] J.W. Rose, Dropwise condensation theory and experiment: a review, Proc. Inst. Mech. Eng. Part A 216 (2002) 115–128.
[21] V. Carey, Liquid–Vapor Phase-Change Phenomena, second ed., Taylor & Francis, New York, 2008.
[22] R. Marek, J. Straub, Analysis of the evaporation coefficient and the condensation coefficient of water, Int. J. Heat Mass Transfer 44 (2001) 39–53.
[23] C. Graham, P. Griffith, Drop size distributions and heat transfer in dropwise condensation, Int. J. Heat Mass Transfer 16 (1973) 337–346.
[24] I.A. Larmour, S.E.J. Bell, G.C. Saunders, Remarkably simple fabrication of superhydrophobic surfaces using electroless galvanic deposition, Angew. Chem. Int. Ed. 46 (2007) 1710–1712.
[25] N.J. Gernert, J. Toth, J. Hartenstine, 100 W/cm^2 and higher heat flux dissipation using heat pipes, in: 13th International Heat Pipe Conference, Shanghai, China, 2004.
[26] T.W. Davis, S.V. Garimella, Thermal resistance measurement across a wick structure using a novel thermosyphon test chamber, Exp. Heat Transfer 21 (2008) 143–154.
[27] A. Tuteja, W. Choi, G.H. McKinley, R.E. Cohen, M.F. Rubner, Design parameters for superhydrophobicity and superoleophobicity, MRS Bull. 33 (2008) 752–758.
[28] M. Kollera, U. Grigull, Über das abspringen von tropfen bei der kondensation von quecksilber (the bouncing off phenomenon of droplets with condensation of mercury), Heat Mass Transfer 2 (1969) 31–35.
[29] A. Nakajima, K. Hashimoto, T. Watanabe, K. Takai, G. Yamauchi, A. Fujishima, Transparent superhydrophobic thin films with self-cleaning properties, Langmuir 16 (2000) 7044–7047.
[30] N. Miljkovic, R. Enright, E.N. Wang, Effect of droplet morphology on growth dynamics and heat transfer during condensation on superhydrophobic nanostructured surfaces, ACS Nano 6 (2012) 1776–1785.
[31] J. Cheng, A. Vandadi, C.L. Chen, Condensation heat transfer on two-tier superhydrophobic surfaces, Appl. Phys. Lett. 101 (2012) 131909.
[32] J.Y. Chang, R.S. Prasher, S. Prstic, P. Cheng, H.B. Ma, Evaporative thermal performance of vapor chambers under nonuniform heating conditions, J. Heat Transfer 130 (2008) 121501.
[33] T. Semenic, I. Catton, Experimental study of biporous wicks for high heat flux applications, Int. J. Heat Mass Transfer 52 (2009) 5113–5121.
[34] R. Chen, M.C. Lu, V. Srinivasan, Z. Wang, H.H. Cho, A. Majumdar, Nanowires for enhanced boiling heat transfer, Nano Lett. 9 (2009) 548–553.
[35] Q. Cai, C.L. Chen, Design and test of carbon nanotube biwick structure for high-heat-flux phase change heat transfer, J. Heat Transfer 132 (2010) 052403.
[36] C. Ding, G. Soni, P. Bozorgi, B.D. Piorek, C.D. Meinhart, N.C. MacDonald, A flat heat pipe architecture based on nanostructured titania, J. Microelectromech. Syst. 19 (2010) 878–884.
[37] J.A. Weibel, S.V. Garimella, J.Y. Murthy, D.H. Altman, Design of integrated nanostructured wicks for high-performance vapor chambers, IEEE Trans. Compon. Pack. Manuf. Technol. 1 (2011) 859–867.
[38] Y. Nam, S. Sharratt, G. Cha, Y.S. Ju, Characterization and modeling of the heat transfer performance of nanostructured Cu micropost wicks, J. Heat Transfer 133 (2011) 101502.
[39] C. Oshman, Q. Li, L.A. Liew, R.G. Yang, Y.C. Lee, V.M. Bright, D.J. Sharar, N.R. Jankowski, B.C. Morgan, Thermal performance of a flat polymer heat pipe heat spreader under high acceleration, J. Micromech. Microeng. 22 (2012) 045018.
[40] C.J. Love, J.D. Smith, Y.H. Cui, K.K. Varanasi, Size-dependent thermal oxidation of copper: single-step synthesis of hierarchical nanostructures, Nanoscale 3 (2011) 4972–4976.